Local energy analysis of high-cycle fatigue using digital image correlation and infrared thermography

Andre Chrysochoos, Bruno Berthel, Félix Latourte, André Galtier, Stéphane Pagano, Bertrand Wattrisse

Local energy analysis of high-cycle fatigue using digital image correlation and infrared thermography

A Chrysochoos[1*], **B Berthel**[1,2], **F Latourte**[1,3], **A Galtier**[2,4], **S Pagano**[1], and **B Wattrisse**[1]
[1]Laboratory of Mechanics and Civil Engineering, University of Montpellier II, Montpellier, France
[2]Arcelor Research SA, Maizières-lès-Metz, France
[3]Department of Mechanical Engineering, Northwestern University, Evanston, IL, USA
[4]CeTIM, Senlis Cedex, France

Abstract: This paper presents the first results provided by an experimental set-up developed to estimate locally the terms of the energy balance associated with the high-cycle fatigue (HCF) of DP 600 steel. The experimental approach involves two quantitative imaging techniques: digital image correlation and infrared thermography. First, a variational method is used to derive stress fields from the displacement fields. Patterns of deformation energy per cycle can then be determined on the basis of stress and strain data. Second, a local form of the heat equation is used to derive separately the thermoelastic and dissipative sources accompanying HCF. Energy balances show that around 50 per cent of the deformation energy associated with the mechanical hysteresis loop is dissipated while the rest corresponds to stored energy variations.

Keywords: image correlation, thermography, deformation work, dissipation, stored energy, fatigue, steel

1 INTRODUCTION

It is well known that standard characterization of fatigue in materials requires time-consuming and statistical processing of the numerous results provided by expensive mechanical tests. Over the last two decades, alternative experimental approaches have been developed to produce reliable fatigue characteristics, including thermal methods based on the analysis of self-heating during stepwise loading fatigue tests, rapidly [**1**–**6**]. Although realistic estimates of these characteristics have sometimes been obtained, the thermal approach often leads to questionable results [**7**]. In previous papers [**8**, **9**], it was emphasized that the direct use of temperature as a fatigue indicator is not always reliable because the temperature variation is not intrinsic to the material behaviour.

*Corresponding author: *Laboratory of Mechancs and Civil Engineering, University of Montpellier II, Place E. Bataillon, Montpellier, 34095 Cedex 05, France. email: chryso@lmgc.univ-montp2.fr*

Therefore, fatigue phenomena were studied using an energy approach with the aim of experimentally determining the deformation energy and the heat distribution accompanying the fatigue test. Naturally, developing an energy analysis of material behaviour is not original in itself. For example, in 1933, Taylor and Quinney [**10**] developed a microcalorimetric analysis of the plastic deformation during monotonic tests. The famous synthesis work written by Bever *et al.* [**11**] in 1973 on the stored energy of cold work must also be mentioned. Studies on the calorimetric effects of cyclic deformation seem to have been fewer in number. Nevertheless the work by Dillon [**12**] in which overall (i.e. on the specimen scale) energy balances during low-cycle fatigue (LCF) (large plastic strain) were proposed should be mentioned. The method presented in reference [**13**] based upon dissipation estimates was developed to determine rapidly the fatigue limit of materials. Overall energy balances were performed in reference [**14**] during high cycle fatigue (HCF) and LCF of metallic materials. Finally, in reference [**15**],

two-dimensional patterns of mean dissipation per cycle during a fatigue crack on a notched specimen were shown. Except for reference [**15**], these previous studies were overall energy approaches to the fatigue phenomena.

This paper presents the first results obtained with an improved combined image-processing method developed to obtain two-dimensional patterns of energy balances. Speckle image correlation techniques, involving a charge-coupled device (CCD) camera [**16**], were used to assess surface displacement fields. These kinematic fields enabled distributions of elastic parameters and stress patterns to be identified by minimizing a given energy functional. In parallel, thermal data were provided by an infrared (IR) focal plane array camera [**17**]. Heat sources were estimated on the basis of partial derivative operators present in a local form of the heat diffusion equation by using a set of approximation functions that locally fits the temperature field and takes the spectral properties of the sought sources into account. Moreover, this approximation enabled us to estimate separately dissipated energy, which came from the irreversible manifestations of microstructural defects, and thermoelastic coupling sources, which were induced by reversible thermal expansion of the crystalline network. Deformation and dissipated energies finally led to an indirect estimate of the distribution of energy stored by the material during HCF. From a modelling point of view, the stored energy variations correspond to internal energy variations induced by microstructural transformations. Generally speaking, these variations and those of thermoelastic sources are directly linked to the thermodynamic potential chosen to describe the material state. Furthermore, experimental dissipation data give valuable information to define a consistent dissipation potential used to derive the evolution laws describing the irreversibility of the fatigue process. Stored and dissipated energies are finally essential safeguards to formulate thermomechanically consistent constitutive equations for fatigue models.

The paper is composed as follows: the different terms of the energy balance associated with HCF of steels are first recalled. A brief review of kinematic and thermal image processing principles is then given and the benefits of their combined use emphasized. Finally, two-dimensional energy fields obtained on dual-phase steel (DP 600) are presented to highlight the promising character of this local energy analysis of fatigue mechanisms.

2 LOCAL FORM OF THE ENERGY BALANCE

From a thermomechanical point of view, fatigue is considered as a dissipative quasi-static process. Within the formalism of the classical thermodynamics of irreversible processes [**18**], the equilibrium state of each volume material element is then described using a set of N state variables. The chosen variables are the absolute temperature T, the linearized strain tensor $\boldsymbol{\varepsilon}$ (small-strain hypothesis), and $N-2$ element vector $\boldsymbol{\alpha}$ which pools the so-called internal variables. These variables describe the macroscopic effects of complex coupled microstructural phenomena.

The rate $w_{\mathrm{def}}^{\bullet}$ of deformation energy per unit volume is classically defined by

$$w_{\mathrm{def}}^{\bullet} = \boldsymbol{\sigma} : \dot{\boldsymbol{\varepsilon}} \tag{1}$$

where $\boldsymbol{\sigma}$ is the Cauchy stress tensor. The symbol $(\,)^{\bullet}$ means that the time variation of $(\,)$ is path dependent (e.g. w_{def} is not a state function *a priori*). The local heat diffusion equation is written as

$$\rho C\dot{T} - \mathrm{div}(\boldsymbol{K}\,\mathrm{grad}T) = d_1 + s_{\mathrm{the}} + s_{\mathrm{ic}} + r_{\mathrm{ext}} \tag{2}$$

where ρ is the mass density, C the specific heat, and $\boldsymbol{K}$ the conduction tensor. The heat sources are, in turn, the intrinsic dissipation d_1, the thermomechanical coupling sources that pool the thermoelastic source s_{the} and the other internal coupling sources s_{ic}, and the external volume heat supply r_{ext}. The volume heat sources d_1, s_{the}, and s_{ic} are related to the specific free energy $\psi(T, \boldsymbol{\varepsilon}, \boldsymbol{\alpha})$ by

$$d_1 = \boldsymbol{\sigma} : \dot{\boldsymbol{\varepsilon}} - \rho\psi_{,\boldsymbol{\varepsilon}} : \dot{\boldsymbol{\varepsilon}} - \rho\psi_{,\boldsymbol{\alpha}}\dot{\boldsymbol{\alpha}} \tag{3a}$$

$$s_{\mathrm{the}} + s_{\mathrm{ic}} = \rho T\psi_{,\mathrm{T}\boldsymbol{\varepsilon}} : \dot{\boldsymbol{\varepsilon}} + \rho T\psi_{,\mathrm{T}\boldsymbol{\alpha}}\dot{\boldsymbol{\alpha}} \tag{3b}$$

Equation (3a) means that the intrinsic dissipation is the difference between the deformation energy rate and the sum of the elastic and stored energy rates. The second-order cross derivatives of the free energy in equation (3b) emphasizes the thermal dependence of the material which induces coupling heat sources. During the fatigue tests, temperature variations remained minimal (less than 15 K) and could not modify the internal state of the material; therefore the corresponding heat sources s_{ic} were neglected and the thermoelastic sources were compared with those given by the classical linear thermoelastic model. The thermoelastic source could then be written as $s_{\mathrm{the}} \approx -\alpha_{\mathrm{d}} T_0\ \mathrm{Tr}\ \dot{\boldsymbol{\sigma}}$, where

α_d is the linear thermal expansion coefficient, T_0 the room temperature, and 'Tr' stands for the trace operator.

3 LOCAL ENERGY ASSESSMENT

The experimental set-up designed for the energy balance construction involves an MTS hydraulic testing machine (frame, 100 kN; load cell, 25 kN), a CEDIP Jade III IR camera and an ATMEL Camelia 8M high-resolution CCD camera. The optical axes of both cameras was set perpendicular to the frame of the testing machine and remained fixed during the test.

The main characteristics of the two cameras are given in Table 1.

3.1 Deformation energy

3.1.1 Digital image correlation metrological aspects

To compute the deformation energy, digital image correlation (DIC) techniques were used. Generally speaking, speckle image processing gives the space–time evolution of various kinematic variables (e.g. displacement, velocity, strain, and strain rate) on the sample surface. In this work, white light was utilized rather than coherent light as it is less sensitive to out-of-plane movements. The camera was carefully set so that the CCD detector remains parallel to the sample surface. Indeed, each out-of-plane movement (translation or rotation) produces a parallax error which distorts the images. In order not to disturb the interpretation of the measurements, it is important to minimize these distortions. Therefore a first positioning was made by a three-axis rotational stage, allowing easy tilt corrections. Then fine adjustments were achieved by vertical translation of the sample in front of the camera. The comparison between strain fields associated with rigid body motions (identically equal to zero) and the strain measurements enabled us to check and optimize the alignment procedure. A typical error on the strain measurements due to the setting up of the camera, was about 1×10^{-4} to 2×10^{-4}.

The image processing was systematically realized after the test into two steps.

First, the displacement field was estimated. The displacement of each point located on the surface of the sample has three components: two in-plane components U and V, and one out-of-plane component W. Only U and V can be directly computed by a two-dimensional digital image correlation algorithm. Fortunately, W is not useful for computing the deformation energy as long as a plane stress state and a homogeneous flow in the depth direction are assumed, which was the case for the thin flat fatigue specimens used.

Second, the strains (or the strain rates) were then derived from the displacements by space (and time) differentiation. Each computational step used a particular numerical processing. A brief summary follows.

The in-plane components of the displacement components U and V are given by maximizing the normalized correlation function φ. This function is computed for translations of integer pixel values. Consequently, the discrete character of φ only allows displacement measurements with 1 pixel resolution. To reach subpixel resolution, a local interpolation is performed in the neighbourhood of the discrete maximum of φ.

To achieve accurate strain measurements, the displacement field is to be filtered before any spatial or temporal differentiation. A fitting technique was chosen based on a local least-squares (linear or quadratic) approximation of the discrete displacement data which also allows the computation of the derivatives. The choice of the approximation zone (AZ) is very important in the differentiation process. The optimized AZ depends on the signal-to-noise ratio and the amplitude of the sought derivatives.

The performances of this image processing were tested on both analytical and experimental cases corresponding to rigid body motions (translation or rotation), or to homogeneous or heterogeneous straining. The influence of all the computation parameters on the displacement and strain measurement was also analysed. Note that DIC is now a widely used experimental technique [**19**–**21**]. The reader interested in the detailed metrological issues of the image processing used in this work can refer to reference [**16**]. In the case of the fatigue tests described hereafter, the absolute uncertainty in terms of displacement measurement was about

Table 1 Main camera characteristics

Camera	Image size (pixel)	Scale factor (μm/pixel)	Frame rate (Hz)
IR CEDIP Jade III	320×240	524	25
CCD: ATMEL Camelia 8M (binning, 4×4)	875×575	136	5

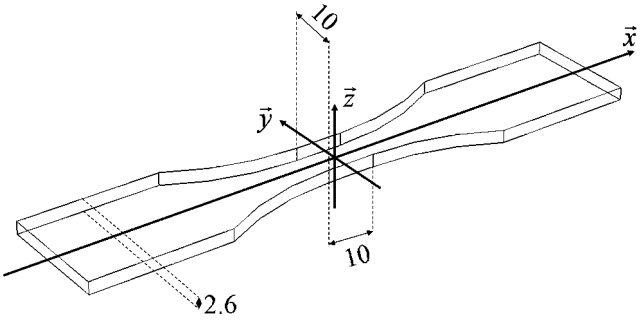

Fig. 1 Shape and main dimensions of the specimen; frame of reference (dimensions are in millimetres)

5×10^{-2} pixels and 1×10^{-4} regarding the strain calculation. Measurement fields were obtained on surfaces totally covering the sample gauge part. The technical drawing of the fatigue specimen is shown in Fig. 1. Specimens were machined in a 2.6 mm thin sheet with a 10 mm length and 10 mm width gauge part.

3.1.2 Variational method

DIC provides in-plane displacement fields and after derivation, fields of small strain ε and strain rate $\dot{\varepsilon}$. A variational method, associated with an elastic energy functional, defined in reference [**22**] was used both to identify the field of elastic parameters and to determine the elastic plane stress pattern $\boldsymbol{\sigma}$. The energy functional F on an appropriate domain of interest Ω (typically the sample gauge part) is given by

$$F(\boldsymbol{\tau},\boldsymbol{B})=\frac{1}{2}\int_{\Omega}[\boldsymbol{\varepsilon}(u)-\boldsymbol{B}:\boldsymbol{\tau}]:\boldsymbol{B}^{-1}:[\boldsymbol{\varepsilon}(u)-\boldsymbol{B}:\boldsymbol{\tau}]\ \mathrm{d}\Omega \quad (4)$$

where the stress field $\boldsymbol{\tau}$ is statically admissible, and where the compliance tensor $\boldsymbol{B}$ (depending on Young's modulus and Poisson's ratio in the case of isotropic elasticity) is supposed to be symmetrical, non-negative, and definite.

The functional $F(\boldsymbol{\tau}, \boldsymbol{B})$ is separately convex and positive, and null at point $(\boldsymbol{\sigma}, \boldsymbol{A})$ if and only if $(\boldsymbol{\sigma}, \boldsymbol{A})$ satisfies the constitutive equations. Therefore the identification is performed by numerically minimizing the functional F. A minimization is performed by a relaxation method which gives the stress field solution and the field of elastic parameters, respectively. During the tests, the overall forces applied at the specimen boundary were recorded. For each loading step, the variational approach provided a couple $(\boldsymbol{\sigma}, \boldsymbol{A})$ where $\boldsymbol{\sigma}$ is a stress tensor and $\boldsymbol{A}$ a compliance tensor. This couple becomes a candidate solution for the identification problem if it satisfies local equilibrium equations, linear elasticity equations, and global equilibrium.

3.1.3 Estimate of the deformation energy rate

Knowledge of the stress and strain rate fields then allows construction of the distributions of deformation energy rate. Since the temperature variations remained small ($|T–T_0|<10$ K, $T_0\approx293$ K) throughout the tests, their influence on the microstructural state (no self-annealing) and on the strain fields was neglected. To estimate $w^{\bullet}_{\mathrm{def}}$, the in-plane components U and V of the displacement field were used. The plane stress hypothesis was assumed to be valid until strong triaxiality effects induced by fatigue localization occur. The microplastic and microdamage effects induced by HCF were then supposed to be taken into account by performing an elastic identification at each loading step. By doing this, it was considered that the stress field on a mesoscopic scale remains close to the elastic field for a given overall loading and a given strain field. This time-consuming operation led to a slight regular adjustment of elastic parameters, enabling the mechanical hysteresis loop to be described.

To check the consistency of the results given by the variational approach, plane stress components were also computed using local equilibrium equations and strain as in reference [**23**]. It was observed that both approaches give similar results. An order of magnitude of the mean relative uncertainty between both types of estimate is about 75 kJ/m^3 for a mean deformation energy rate per cycle of about 1500 kJ/m^3 (see reference [**24**] for more details).

Then, stress and strain field measurements were used to compute the mean volume energy rate corresponding to the hysteresis A_{h} according to

$$A_{\mathrm{h}}(x,y)=\int_0^{f_{\mathrm{L}}^{-1}}\sigma_{ij}(x,y,t)\dot{\varepsilon}_{ij}(x,y,t)\ \mathrm{d}t=w_{\mathrm{def}}(x,y) \quad (5)$$

where f_{L} is the loading frequency. The hysteresis area indeed represents the deformation energy finally spent in a cycle at given fatigue state (i.e. a given number of cycles, or a given block of cycles, for a given loading history).

3.2 Heat sources

3.2.1 Infrared metrology

A stable and spatially uniform IR radiation source must be used to perform the camera signal

calibration. Therefore a planar black-body SR 80-4A (by CI Systems) with the following main specifications was used: accuracy ($\pm 0.008\,^{\circ}$C for $5\,^{\circ}$C temperature amplitude), thermal resolution ($\delta T_R = 0.01\,^{\circ}$C), and spatial non-uniformity of the target (less than $\pm 0.02\,^{\circ}$C).

Standard calibrations are based on a non-uniformity correction (NUC) operation that assumes a linear response of each detector element [**17**]. First, this condition may limit the thermal range used for the calibration or may induce uncontrolled errors if some elements start to behave non-linearly. Second, even if all element responses remain linear, the standard calibration protocol replaces some bad pixels because their responses are far from the mean detector response (bad pixel replacement (BPR) operation). In the framework of thermomechanical applications, this replacement operation may distort the thermal gradient computation by spatially correlating measurement errors. This distortion consequently affects the heat source estimate. These are the main reasons why a new protocol based on individual calibration of detector elements has been proposed. It is possible to short cut NUC and BPR operations with the infrared thermography (IRT) workstation used in this study. This feature was used to develop an individual pixel calibration based on polynomial fitting of the temperature as a function of the signal delivered by the *i*th element of the detector when the camera is placed in front of the black-body source at different temperatures. Generally polynomials of degree greater than 5 are chosen. When the difference between the temperature of a pixel, deduced from the calibration, and the black-body temperature is greater than a given threshold (equal here to 40 mK), it is considered to be defective. Typically, 0.3 per cent of bad pixels are identified on the camera used in this study. They are rather randomly distributed over the detector surface. Nevertheless several bad pixel packs could be observed.

Naturally, other parameters may cause the quality of the temperature measurements to degrade (thermal drift, parasitic radiation emanating from the lenses, etc). Readers interested in these metrological issues can consult reference [**17**]. To conclude temporarily with problems of IR metrology, the peak-to-peak thermal noise was estimated to be about 200 mK (i.e. before data filtering) and the range of the thermal noise dropped to 2 mK for standard filtering parameters. Moreover, the order of magnitude of the spatial resolution was about 0.16 mm and the temporal resolution was considered to be equal to the $f_s^{-1}(\approx 0.05$ s) acquisition period used in the fatigue tests.

3.2.2 *Estimate of the heat source*

The overall heat source can be theoretically estimated by evaluating the left-hand side of the heat equation (equation (2)). Nevertheless, the only thermal information given by the IR camera is surface temperature fields. The heat source evaluation throughout the specimen gauge part (three-dimensional inverse problem) is an ill-posed problem that is impossible to solve without any complementary information.

The regularizing effects of heat diffusion fortunately limit the thermal gradients throughout the (small) thickness of the specimen (Fig. 1). In particular, four of the present authors [**17**] previously established that thermal data on the surface remain close to the average temperature during cyclic tests. This result warranted the use of an integrated form of the heat equation over the sample thickness to estimate the depthwise-averaged heat source distribution. The following assumptions were also made to perform the heat source evaluation.

1. The conduction tensor $\boldsymbol{K}$ is isotropic and the related coefficient k remains constant during the test.
2. The parameters ρ and C are material constants, independent of the internal state.
3. The convective terms included in the material time derivation are neglected.
4. The external heat supply r_{ext} (here due only to radiation heat exchanges) is time independent. Consequently, the equilibrium temperature field T_0 verifies that $-k\,\Delta T_0 = r_{ext}$.

Under these hypotheses and, first, assuming symmetrical linear heat exchanges between the front specimen faces and the surroundings and between the back specimen faces and the surroundings, second, integrating equation (2) over the sample thickness, and, third, assuming that the thermal image is very close to the depthwise-averaged temperature field, the two-dimensional equation can be obtained as

$$\rho C\left(\frac{\partial \bar{\theta}}{\partial t} + \frac{\bar{\theta}}{\tau_{th}}\right) - k\,\Delta\bar{\theta} = \bar{d}_1 + \bar{s}_{the} \tag{6}$$

where $\bar{\theta}$ is the depthwise-averaged temperature variations, k is the isotropic conduction coefficient, and $\bar{d}_1$ and $\bar{s}_{the}$ are the dissipation and thermoelastic source respectively, averaged over the sample thickness. The

symbol τ_{th} stands for a time constant characterizing heat losses perpendicular to the plane of the specimen by convection, conduction, and radiation, while heat conduction in the plane is taken into account by the two-dimensional Laplacian operator.

Construction of the heat source distribution via equation (6) requires the evaluation of partial derivative operators applied to noisy digital signals. To compute reliable estimates of heat sources, it is then necessary to reduce the noise amplitude without modifying the spatial and temporal thermal gradients. Among several possible methods, a special local least-squares fitting of the thermal signal was considered for the calorimetric fatigue analysis [**9**, **17**]. The temperature approximation functions account for the spectral properties of the underlying heat sources. Moreover, the linearity of equation (3) and that of the respective boundary conditions enabled us to analyse separately the influence of thermoelastic and dissipative heat sources. Within the linear thermoelasticity framework, it is easy to verify, first, that the thermoelastic source has the same frequency spectrum as the stress signal and, second, that the variation in the thermoelastic energy w_{the} vanishes at the end of each loading cycle of period f_L^{-1}. Regarding the dissipative effects, the dissipation averaged over a whole number n of complete cycles (e.g. n is the number of cycles per second), $\tilde{d}_1 = \int_{nf_L^{-1}} n^{-1} f_L \bar{d}_1 \, d\tau$, was considered. The new variable $\tilde{d}_1$ is sufficient to characterize the slow changes in the material microstructure due to fatigue phenomena. The average dissipation $\tilde{d}_1$ per cycle is thus a positive heat source whose spectrum is limited to very low frequencies.

Henceforth by denoting $\overline{\Delta s}_{the}$ as the range of the thermoelastic source averaged over n cycles, the aim of the image processing is to assess $\overline{\Delta s}_{the}$ and $\tilde{d}_1$ separately. The latter characterizes the slow degradation of the material microstructure due to fatigue phenomena including diffuse microplasticity, development of localized persistent slip bands (PSBs), and progressive damage growth leading to microcracks while the second is associated with the reversible thermodilatability of the material and should indicate possible interactions between microplasticity, fatigue damage, and elastic properties.

The local fitting function θ^{fit} of the temperature charts was chosen as

$$\begin{aligned}\theta^{fit}(x,y,t) = {} & p_1(x,y)t + p_2(x,y) \\ & + p_3(x,y)\cos(2\pi f_L t) \\ & + p_4(x,y)\sin(2\pi f_L t)\end{aligned} \tag{7}$$

where the trigonometric time functions describe the periodic part of the thermoelastic effects while the linear time function takes transient effects due to heat loss, dissipative heating, and possible drift in the equilibrium temperature into account. The functions $p_i(x, y)$, $i = 1, \ldots, 4$, are second-order polynomials in x and y. These polynomials enabled us to take possible spatial heterogeneities in the source patterns into account. The efficiency of the local fitting of the temperature field can be estimated by considering the temperature difference $\delta\theta_{ijk}$ between the noisy measurements $\theta_{ijk}^{exp} = \theta^{exp}(x_i, y_j, \tau_k)$ and the fitted values $\theta_{ijk}^{fit} = \theta^{fit}(x_i, y_j, \tau_k)$. Take, for example, the following standard situation where the approximation data groups (21×21) pixels $\times$ 57 frames (corresponding to recording for 3 s at $f_S = 19$ Hz). For such an example, the mean absolute error $\bar{E}_{\delta\theta} = \langle \delta\theta \rangle$ is less than 10^{-12} °C while the standard deviation $\sigma_{\delta\theta}$ is about 0.030 °C. These estimates were made by using a set of experimental noisy thermal data extracted from a real fatigue test. Also, the noise in the IR measurements was characterized by a centred Gaussian distribution with a standard deviation of 0.027 °C. These results show that the approximation function set is convenient to construct correctly a denoised temperature signal.

4 EXPERIMENTAL RESULTS

The material under examination is DP 600 steel produced by Arcelor (dual-phase carbon steel). This material is a hot-rolled steel grade containing ferrite and martensite. It is composed of 0.074 wt % C, 0.84 wt % Mn, 0.038 wt % P, 0.002 wt % S, 0.217 wt % Si, 0.04 wt % Al, 0.702 wt % Cr, and 0.005 wt % N. The thermophysical properties of DP 600 are the following: mass density $\rho = 7800$ kg/m^3; heat capacity $C = 460$ J/kg K; isotropic heat conduction coefficient $k = 64$ W/m K; linear thermal expansion coefficient $\alpha_d = 10 \times 10^{-6}$ K^{-1}. The standard mechanical properties are the following: Young's modulus $E = 213$ GPa; yield stress $\sigma_{0.2\%} = 401$ MPa; ultimate tensile stress $\sigma_u = 611$ MPa. The fatigue limit $\Delta\sigma_\infty$ obtained at 2×10^6 cycles at loading ratio $R_\sigma = \sigma_{min}/\sigma_{max} = -1$ is about 526 MPa.

The tests involved two series of five short loading blocks ($N_c = 2400$ cycles) performed at increasing stress range $\Delta\sigma$ (180 MPa $< \Delta\sigma <$ 570 MPa) with a constant stress ratio $R_\sigma = -1$ and a constant loading frequency $f_L = 30$ Hz. Between the two series, a block of 100 000 cycles was completed with the maximum

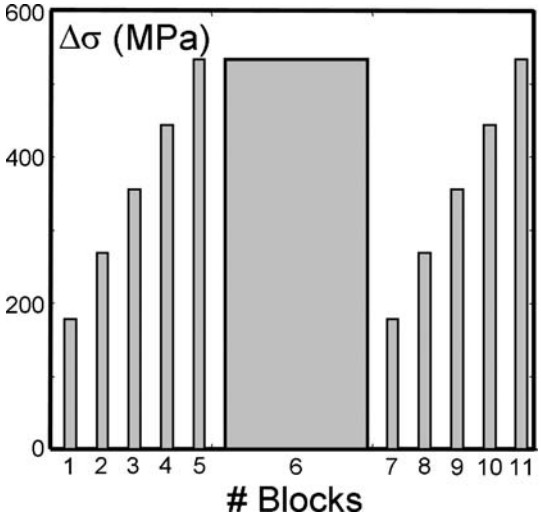

Fig. 2 Series of blocks: short blocks, 2400 cycles; long block, 100 000 cycles

stress range nearly corresponding to $\Delta\sigma_\infty$. Figure 2 illustrates the sequences of blocks associated with the test. The shorter blocks allowed estimation of the dissipation levels at different stress amplitudes and at relatively constant damage state whereas the longer block (in the maximum constant stress range) aimed at speeding up the fatigue development. At the end of each block, a cycle was completed at a lower loading frequency ($f_L = 5.55\times10^{-3}$ Hz). During this last cycle, displacement fields were then provided for the identification procedure determining local elastic tensors, and plane stress patterns. In addition, the calorimetric analysis showing that the energy dissipated in a cycle was independent of the loading frequency [**25**, **26**]; it was assumed that the deformation energy corresponding to the hysteresis loop of the stress–strain curve was also rate independent. It should be emphasized that this important hypothesis is fully consistent with a thermoelastic–plastic–damageable behaviour.

The following results are associated with complete local energy balances performed on a single specimen. Nevertheless, the techniques of deformation and dissipated energy assessments where separately applied on numerous specimens, loadings, and materials. In all cases, similar trends were observed what showed the reproducibility of energy mechanisms.

4.1 Identification of elastic parameters and stress patterns

First, the results derived from the identification procedure are presented. Using the variational inverse method, the distribution of elastic parameters was obtained. Figure 3 shows the progression of the averaged Young's modulus $\langle E\rangle$ and Poisson's ratio $\langle \nu\rangle$ over the identification domain during a complete loading cycle ($f_L = 5.55\times10^{-3}$ Hz). For small levels of applied load, the signal-to-noise ratio on strain measurements is poor, and consequently the identification results were inaccurate. For higher load levels, the identified values were stable. It was estimated that for load levels lower than the threshold load $F_{min} = 2.5$ kN and corresponding to a macroscopic strain level of 4×10^{-4}, slightly higher than the resolution of the strain measurement, the identified material properties could not be estimated precisely. Averaging the representative values over the loading cycle, $\langle E\rangle_{cycle} = 215$ GPa and $\langle \nu\rangle_{cycle} = 0.3$ were obtained. Furthermore, slight and regular variations in the identified elastic moduli can be observed during the loading cycle. These variations were interpreted as the result of couplings between elasticity and microplasticity which slightly modified the identified secant

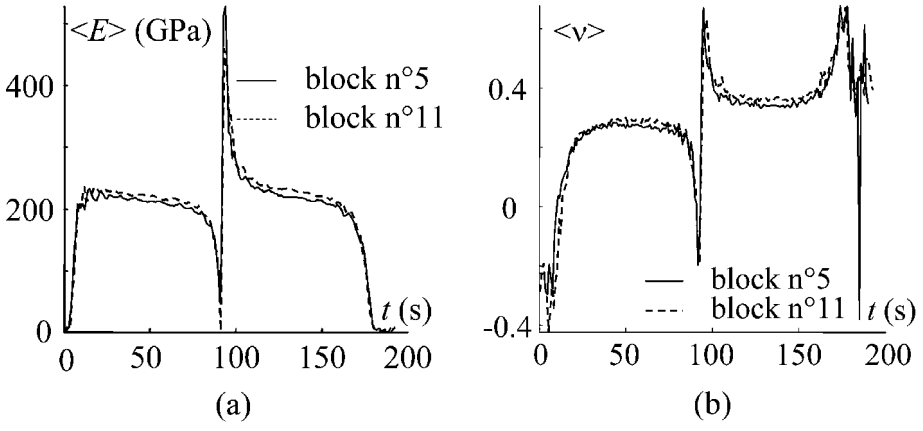

Fig. 3 Identification of (a) Young's modulus and (b) Poisson's ratio

compliance tensor. Results associated with blocks 5 and 11 do not show a clear influence of fatigue damage on the elastic parameters.

This undetected influence between both blocks may be quite surprising since fatigue mechanisms are often interpreted in terms of damage coupled with elasticity and plasticity [**27**, **28**]. The high endurance qualities of DP 600 (made for technical parts subjected to fatigue) and the small number of loading cycles performed (less than 125 000) could explain here the low influence of damage.

Figure 4 shows the fields of elastic properties identified after blocks 5 and 11 and averaged over the loading cycle for $|F| \geqslant F_{\min}$. The material coefficients are determined on a regular mesh constituted by 10×10 elements centred in the middle of the sample gauge part.

The distributions of elastic parameters are quite homogeneous; standard deviations are smaller than 4 GPa for Young's modulus and 0.014 for Poisson's ratio. This represents around 5 per cent of spatial variations. Nevertheless, these small variations can be interpreted as deterministic gradients since similar patterns of identified parameters are derived throughout the test. This can be verified by closely comparing Figs 4(a) and (b) and then Figs 4(c) and (d). The noisy nature of displacement data and the unstable character of inverse identification methods make the interpretation of such results quite delicate. However, it should be emphasized that steady gradients of material properties could naturally come from uncontrolled systematic errors of the image processing but they also could be induced by heterogeneity of the material state. Knowledge of the initial heterogeneity of the material state could become essential to improving the understanding and mastering of the random response of fatigue specimens which has led several workers to model HCF as random phenomena (see, for example, references [**29**] and [**30**]). Supplementary tests have to be developed to check the reliability of this key conjecture.

The identification method also provided the plane stress distributions that are essential to compute the deformation energy associated with a mechanical hysteresis loop. Figure 5 shows the distributions of the plane stress components, captured at $F_{\min}$ (yield load) and $F_{\max}$ (maximum load) of the cycle associated with blocks 5 and 11.

In all cases, Fig. 5 shows that transverse stresses σ_{yy} and shear stresses σ_{xy} remained low compared with the tensile stresses σ_{xx}, as expected for a so-called uniaxial tensile test.

Furthermore, stress patterns are very similar regardless of the applied load ($F_{\min}$, $F_{\max}$) and the considered block (blocks 5 and 11). This feature is in agreement with the identification of the elastic parameters in the sense that stress patterns seem to be independent of the loading history and then might account for the material heterogeneity. Finally, despite the low shear stresses, some concentrations of σ_{xy} seem to appear in the upper and lower parts of the analysed domain which correspond to the connection zones of the sample.

4.2 Analysis of energy balances

Preliminary two-dimensional energy fields obtained by using both imaging techniques are now presented. Dividing the volume energy by the volume heat capacity ρC of the material gives the volume

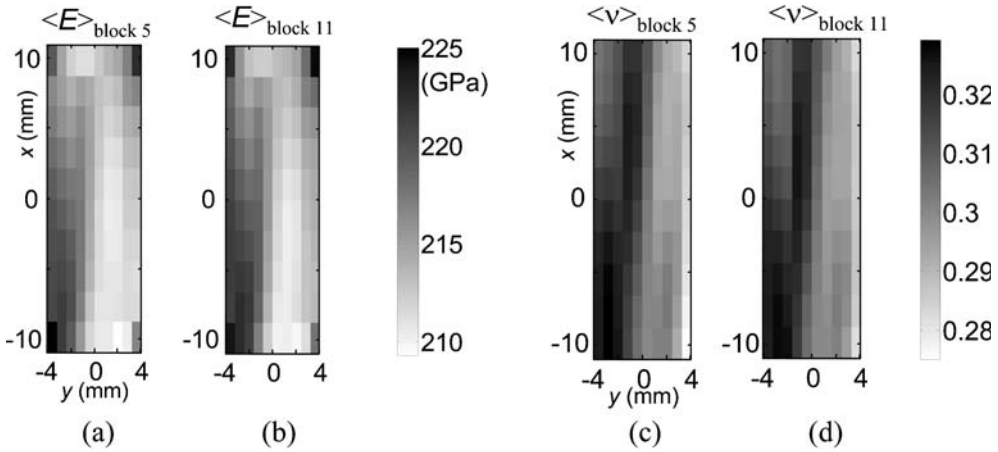

Fig. 4 Averaged elastic parameters over a loading cycle: (a) Young's modulus associated with block 5; (b) Young's modulus associated with block 11; (c) Poisson's ratio associated with block 5; (d) Poisson's ratio associated with block 11

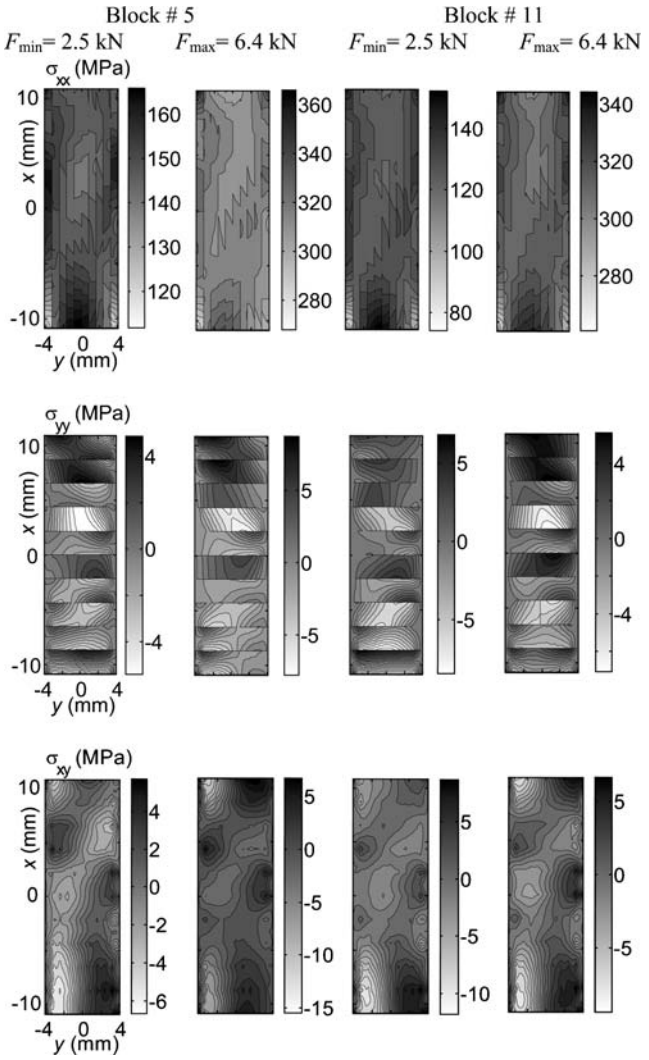

Fig. 5 Plane stress patterns captured at F_{min} and F_{max} for blocks 5 and 11

energy expressed in degrees Celsius. This operation is convenient because it associates an equivalent heating in adiabatic conditions and then gives orders of magnitude of this energy in units easy to grasp. The deformation energy on a cycle was computed by using the stress and strain data (see equation (5)). The distribution of dissipated energy was averaged over the last 120 cycles of the block. It has already been mentioned in reference [**9**] that these averaged values are representative of the slow development of irreversible fatigue phenomena. The computation of the dissipation is made by using the local analytical expression of the fitted thermal data. A detailed presentation of the passage from temperature variation to heat source derivation can be found in references [**9**] and [**17**].

The stored energy is defined as the difference between the deformation energy spent in a cycle and the energy dissipated during this cycle. Indeed, it has been mentioned that equation (3) shows that intrinsic dissipation d_1 is the difference between the deformation energy rate $w_{def}^{\bullet}$ and the sum $w_e^{\bullet} + w_s^{\bullet}$ of the elastic and stored energies. Integrated over a complete loading cycle, equation (3a) shows that the deformation energy w_{def} can be split into the dissipated energy w_d and the stored energy w_s, the elastic energy w_e vanishing at the end of each load–unload cycle. Figure 6 shows the energy balances associated with block 5 and block 11.

An initial overview of Fig. 6 shows that the mean deformation energy over a cycle (around 14×10^{-3} °C) is roughly made up of 50 per cent of dissipated energy and 50 per cent of stored energy. At this level the work of Kaleta [**14**], which showed similar results on the specimen scale, should be mentioned.

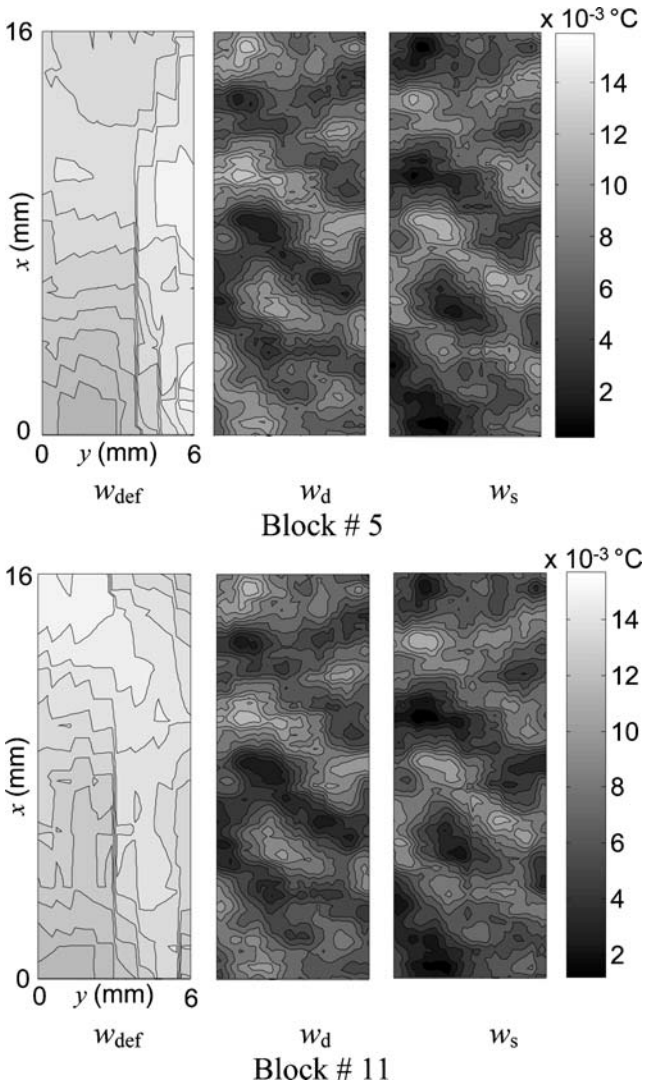

Fig. 6 Fields of the mean energy balances associated with a cycle of block 5 and of block 11

Indeed, in the case of ferritic–perlitic steel, he observed stored energy ratios associated with the stress–strain hysteresis loop varying from 37.4 per cent for LCF tests, and up to 67.3 per cent for HCF tests. In aluminium alloys, stored energy ratios were estimated from 10 per cent to 20 per cent in other work [**31**, **32**].

An accurate observation of Fig. 6 shows a more complicated situation induced by a heterogeneous distribution of the different energies. The heterogeneous character of the dissipation fields induced by HCF has already been emphasized [**9**]. Here, the dissipated and stored energies vary in an initial close approximation between 4×10^{-3} °C and 8×10^{-3} °C.

The last point that should be mentioned is related to the comparison between both energy balances. It can be observed that patterns of dissipated and stored energy associated with block 5 and block 11 are very similar. This kind of feature has already been observed for dissipation fields and it has been emphasized that high dissipation zones represent potential zones where a fatigue crack may occur [**9**]. Here the heterogeneous response of the material in terms of stored energy must also be mentioned. Only the time-consuming image processing prevented continuation of the fatigue test until crack inception. However, it will be interesting also to characterize these potential crack zones in terms of stored energy evolution.

5 CONCLUDING COMMENTS

In this paper, we presented a combined application of DIC and IRT to the fatigue of DP 600 steel. Kinematic and thermal data were used to estimate the deformation energy and the mean dissipated energy per cycle. The deformation energy distribution was computed using strain field measurements, while the stress fields were estimated using a variational inverse method. The heat source distributions were derived from thermal data using a local expression of the heat equation. The linearity of the diffusion equation and that of the thermal boundary conditions enabled the sources to be estimated separately. Finally, the preliminary two-dimensional identified fields obtained with DP 600 steel specimen were presented. The analysis did not reveal any noticeable influence of HCF on the elastic properties (test limited to around 1.5×10^5 cycles). It was also observed that the distribution of mean deformation energy rates per cycle was relatively homogeneous while the image processing showed that dissipation localized since the very beginning of the test. A quasi-homogeneity of the volume deformation energy is observed on the scale imposed by the optical systems and the image processing. Homogeneity seems to be natural since stress and strain gradients should theoretically vanish on this scale for a uniform cyclic tensile test. In the same way, the heterogenous distribution of dissipation can also be explained since PSBs develop gradually in some favourably oriented grains. The wavelength spectrum of this distribution is such that the 'dezoom' leading to the observation scale is not sufficient to make an averaged value representative of the PSB distribution. Consequently, the observed distribution of dissipation remains heterogeneous, the high dissipation zones corresponding to high concentrations of PSBs. Furthermore, image processing showed that the amounts of deformation energy corresponding to the stress–strain hysteresis loop were equally stored and dissipated. This finding could also have a marked impact on the modelling of steel fatigue kinetics; therefore these preliminary results must, as usual, be considered with precaution. Complementary checks and tests should be performed in the near future. Nevertheless, the promising results obtained with the local energy approach, combining DIC with IRT, are already most encouraging.

ACKNOWLEDGEMENTS

The authors would like to thank Arcelor Research SA and Nippon Steel Corporation for their technical and financial support during this study. The authors, members of the Laboratoire de Mécanique et Génie Civil de Montpellier, would also like to thank the Arcelor Fatigue Working Group warmly for fruitful and animated scientific discussions.

REFERENCES

1 **Galtier, A.** *Contribution à l'étude de l'endommagement des aciers sous sollicitations uni ou multiaxiale*. PhD Thesis, Ecole Nationale Supérieure d'Arts et Métiers, Bordeaux, 1993.

2 **Luong, M. P.** Fatigue limit evaluation of metals using an infrared thermographic technique. *Mechanics Mater.*, 1998, **28**, 155–163.

3 **La Rosa, G.** and **Risitano, A.** Thermographic methodology for rapid determination of the fatigue limit of materials and mechanical components. *Int. J. Fatigue*, 2002, **22**(1), 65–73.

4 **Liaw, Y. B., Wang, P. K., Jiang, L., Huang, J. Y., Kuo, R. C.,** and **Huang, J. C.** Thermographic investigation of the fatigue behaviour of reactor

pressure vessel steels. *Mater. Sci. Engng A*, 2001, **314**, 131–139.

5 **Krapez, J. C., Pacou, D.,** and **Gardette, G.** Lock-in thermography and fatigue limit of metals. In Proceedings of the Fifth International Conference on *Quantitative Infrared Thermography (QIRT 2000)*, Reims, France, 8–21 July 2000, pp. 277–282 (QIRT, Lodz, Poland).

6 **Krapez, J. C.** and **Pacou, D.** Thermographic detection of damage initiation during fatigue tests. *Thermosense XXIV*, Proceedings of the SPIE, Vol. 4710, Orlando, Florida, USA, 1–5 April 2002, pp. 435–449 (SPIE, Bellingham, Washington).

7 **Cugy, P.** and **Galtier, A.** Microplasticity and temperature increase in low carbon steels. In Proceedings of the Eighth International Fatigue Congress, Stockholm, Sweden, 2–7 June 2002, pp. 549–556 (EMAS Publishing, Warrington).

8 **Mabru, C.** and **Chrysochoos, A.** Dissipation et couplages accompagnant la fatigue des matériaux métalliques. In *Photomécanique 2001*, Poitiers France, 24–26 April 2001, pp. 375–382 (GAMAC, Paris).

9 **Boulanger, T., Chrysochoos, A., Mabru, C.,** and **Galtier, A.** Calorimetric and thermoelastic effects associated with the fatigue behavior of steels. *Int. J. Fatigue*, 2004, **26**, 221–229.

10 **Taylor, G. I.** and **Quinney, M. A.** The latent energy remaining in a metal after cold working. *Proc. R. Soc. A*, 1933, **143**, 307–326.

11 **Bever, M. D., Holt, D. L.,** and **Titchener, A. L.** The stored energy of cold work. *Prog. in Mater. Sci.*, 1973, **17**(1), 5–177.

12 **Dillon, O. W.** The heat generated during the torsional oscillation of copper tubes. *Int. J. Solids Structs*, 1966, **2**(2), 181–204.

13 **Harry, R., Joubert, F.,** and **Gomaa, A.** Measuring the actual endurance limit of one specimen using a non-destructive method. *Trans. ASME J. Engng Mater. Technol.*, 1980, **103**(1), 71–76.

14 **Kaleta, J.** Determination of cold work energy in LCF/HCF region. In Proceedings of the Fourth International Conference on *Low Cycle Fatigue and Elastoplastic Behaviour of Materials*, Garmisch-Partenkirchen, Germany, 7–11 September 1998, pp. 93–98 (Elsevier, Oxford).

15 **Nayroles, B., Bouc, R., Caumon, H.,** and **Chezeaux, J. C.** Téléthermographie infrarouge et mécanique des structures. *Int. J. Engng Sci.*, 1981, **19**, 929–947.

16 **Wattrisse, B., Chrysochoos, A., Muracciole, J.-M.,** and **Nemoz-Gaillard, M.** Analysis of strain localisation during tensile test by digital image correlation. *J. Expl Mechanics*, 2000, **41**(1), 29–38.

17 **Berthel, B., Chrysochoos, A., Wattrisse, B.,** and **Galtier, A.** Infrared image processing for the calorimetric analysis of fatigue phenomena. *Exp. Mechanics*, 2008, **48**(1), 79–90.

18 **Germain, P., Nguyen, Q. S.,** and **Suquet, P.** Continuum thermodynamics. *J. Appl. Mechanics*, 1983, **50**, 1010–1020.

19 **Chu, T. C., Ranson, W. F., Sutton, M. A.,** and **Peters, W. H.** Application of digital-image-correlation techniques to experimental mechanics. *J. Expl Mechanics*, 1985, **25**, 232–244.

20 **Bruck, H. A., McNeill, S. R., Sutton, M. A.,** and **Peters, W. H.** Digital image correlation using Newton–Raphson method of partial differential correction. *J. Expl Mechanics*, 1989, **31**, 261–267.

21 **Choi, S.** and **Shah, S. P.** Measurement of deformations on concrete subjected to compression using image correlation. *J. Expl Mechanics*, 1997, **37**, 307–313.

22 **Geymonat, G., Hild, F.,** and **Pagano, S.** Identification of elastic parameters by displacement field measurement. *C.R. Mécanique*, 2002, **330**, 403–408.

23 **Latourte, F., Chrysochoos, A., Pagano, S.,** and **Wattrisse, B.** Elastoplastic behavior identification for heterogeneous loadings and materials. *Expl Mechanics*, 2008, **313**. DOI:10.1007/s11340-007-9088-y.

24 **Chrysochoos, A., Berthel, B., Latourte, F., Pagano, S., Wattrisse, B.,** and **Weber, B.** Local energy approach to steel fatigue. *Strain*, 2007, **43**, 273–279. DOI:10.1111/j.1475-1305.

25 **Morabito, A. E., Chrysochoos, A., Dattoma, V.,** and **Galietti, U.** Analysis of heat sources accompanying the fatigue of 2024 T3 aluminium alloys. *Int. J. Fatigue*, 2007, **29**, 977–984.

26 **Berthel, B., Galtier, A., Wattrisse, B.,** and **Chrysochoos, A.** Fatigue dissipation properties of steel sheets. *Strain*, 2007, **43**(3), 273–279.

27 **Lemaitre, J.** *Course on damage mechanics*, 1992 (Springer-Verlag, Berlin).

28 **Charkaluck, E.** and **Constantinescu, A.** Estimation of thermoplastic dissipation in high cycle fatigue. *C.R. Mécanique*, 2006, **334**(6), 373–379.

29 **Doudard, C., Hild, F.,** and **Calloch, S.** A propabilistic model for multiaxial high cycle fatigue. *Fatigue Fracture Engng. Mater. Structs*, 2007, **30**, 107–114.

30 **Doudard, C., Poncelet, M., Calloch, S., Boué, C., Hild, F.,** and **Galtier, A.** Determination of an HCF criterion by thermal measurements under biaxial cyclic loading. *Int. J. Fatigue*, 2007, **29**, 748–757.

31 **Wong, A. K.** and **Kirby III, G. C.** A hybrid numerical/experimental technique for determining the heat dissipated during low cycle fatigue. *Engng Fracture Mechanics*, 1990, **37**(3), 493–504.

32 **Harvey II, D. P.** and **Bonenberger Jr, R. J.** Detection of fatigue macrocracks in 1100 aluminium from thermomechanical data. *Engng Fracture Mechanics*, 2000, **65**, 609–620.